



105  
685  
THS

**LIBRARY**  
**Michigan State**  
**University**

This is to certify that the

thesis entitled

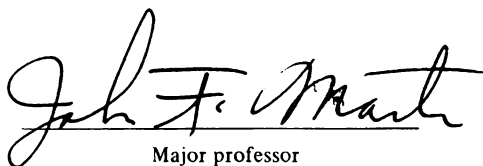
MACROSCOPIC AND MICROSCOPIC STRAIN-LIFE  
BEHAVIOR OF PEARLITIC MALLEABLE IRON

presented by

JOHN SAMUEL CUCCIO JR.

has been accepted towards fulfillment  
of the requirements for

MASTER degree in MATERIALS SCIENCE

  
Major professor

Date 3/20/84



RETURNING MATERIALS:

Place in book drop to  
remove this checkout from  
your record. FINES will  
be charged if book is  
returned after the date  
stamped below.

--	--	--

**MACROSCOPIC AND MICROSCOPIC STRAIN-LIFE  
BEHAVIOR OF PEARLITIC MALLEABLE IRON**

**By**

**JOHN SAMUEL CUCCIO JR.**

**A THESIS**

**Submitted to  
Michigan State University  
in partial fulfillment of the requirements  
for the degree of**

**MASTER OF SCIENCE**

**Department of Metallurgy, Mechanics and Materials Science**

**1984**



## ABSTRACT

### MACROSCOPIC AND MICROSCOPIC STRAIN-LIFE BEHAVIOR OF PEARLITIC MALLEABLE IRON

BY

JOHN SAMUEL CUCCIO JR.

Microscopic and macroscopic behavior for four hardness ranges of pearlitic malleable iron is correlated with the matrix properties and the morphology of the graphite nodules. An analysis of the stress-strain and strain-life behavior is performed. The effects of microscopic discontinuities are characterized with an interferometric strain gage that measured strains over gage lengths varying from 70 to 180  $\mu\text{m}$ . The microstrains are used with Nueber's rule to determine stress concentrations produced by local regions of shrinkage pits and nodules. It was found that the macroscopic strain-life behavior for these four hardness groups is predominantly controlled by the stable cyclic stress-strain response of the matrix. Stress concentrations from the microscopic discontinuities were found to be relatively constant for the two extremes in hardness ranges.

## ACKNOWLEDGEMENTS

I would like to thank the people at General Motors Central Foundry for their assistance throughout this program. I would also like to thank Matt Melis and Barry Spletzer for their help, and for making it fun to work in the lab. My sincere thanks to my advisor and friend, Dr. John Martin, who helped push me to a new level of professional ability.

My deepest love and thanks to my wife who was always there when I needed her.



## TABLE OF CONTENTS

	Page
LIST OF TABLES . . . . .	iv
LIST OF FIGURES . . . . .	v
Chapter 1 INTRODUCTION . . . . .	1
Chapter 2 MATERIAL . . . . .	3
Chapter 3 STRAIN-LIFE TESTS . . . . .	8
3.1 Procedure . . . . .	8
3.2 Observations . . . . .	9
3.3 Data . . . . .	11
3.4 Results . . . . .	17
Chapter 4 ANALYSIS OF STRESS CONCENTRATIONS . . . . .	32
4.1 Test procedure . . . . .	32
4.2 Remote and Local Behavior . . . . .	36
4.3 Nueber application . . . . .	42
Chapter 6 CONCLUSION . . . . .	46
LIST OF REFERENCES . . . . .	48



# LIST OF TABLES

Table		Page
1	Specimen tested . . . . .	4
2	Strain-life data . . . . .	15
3	Strain-life properties . . . . .	31
4	Matrix hysteresis data . . . . .	37
5	Cyclic stress-strain parameters for the matrix . . . . .	39
6	Local strains, local stresses and stress concentrations around discontinuities . . . . .	43



## LIST OF FIGURES

Figure		Page
1	Etched and unetched microstructures . . . . .	6
2	Machined test surface . . . . .	7
3	Microshrinkage . . . . .	7
4	Strain/time sine wave . . . . .	7
5	Specimen schematic . . . . .	9
6	Failure surface . . . . .	10
7	Schematic of a hysteresis loop with parameters . . . . .	12
8	Hysteresis loops from 250 and 230 BHN specimens . . . . .	13
9	Hysteresis loops from 200 and 170 BHN specimens . . . . .	14
10	Log-stress/ log-plastic strain schematic . . . . .	17
11	Cyclic stress-strain curves . . . . .	19
12	Log-stress/log-plastic strain lines . . . . .	20
13	Schematic of strain-life curve with parameters . . . . .	22
14	Strain-life curve for 170 BHN specimens . . . . .	24
15	Strain-life curve for 200 BHN specimens . . . . .	25
16	Strain-life curve for 230 BHN specimens . . . . .	26
17	Strain-life curve for 250 BHN specimens . . . . .	27
18	Total strain-life curves . . . . .	28
19	Elastic strain-life curves . . . . .	29
20	Plastic strain-life curves . . . . .	30





21	Hysteresis loops recorded from interferometric strain measurements . . . . .	33
22	Test regions with indentations . . . . .	34
23	Replicas of discontinuities with indentations . . . . .	35
24	Schematic of remote and local regions . . . . .	36
25	Cyclic stress-strain curve from the matrix . . . . .	38
26	Micrograph of replicas from specimen tested at $\pm 0.3\%$ $\epsilon$ and $\pm 0.14\%$ $\epsilon$ . . . . .	40
27	Hysteresis loops recorded near 1000 cycles . . . . .	41
28	Theoretical stress concentrations from an ellipsoidal cavity . . . . .	44



## CHAPTER 1

### INTRODUCTION

Extensive studies of the mechanical properties of gray and nodular cast iron have been performed<sup>(1-3)</sup>. Very little fatigue data for pearlitic malleable iron has been produced. This thesis study presents a complete set of strain-life data for four hardness ranges (170, 200, 230 and 250 BHN) of pearlitic malleable iron, and characterizes the microstructural effects which produce this response.

Some interest in studying cast irons is inherent in their microstructures. Cast irons are essentially steels with discontinuities. These discontinuities are graphite flakes or nodules, inclusions, and shrinkages. Many of the studies have been directed toward the graphite because it is the predominate discontinuity (by volume), and its morphology can be controlled<sup>(4)</sup>. Since graphite has nearly no strength, as compared with the matrix, it is modeled as a cavity. The effect the microstructure has on the mechanical properties of cast irons can therefore be characterized by determining the mechanical properties of the matrix and the stress concentrations produced by the graphite. The mechanical properties of the matrix can be estimated by comparing it to a cast steel with a similar microstructure and hardness. Stress concentrations produced by the graphite can be estimated by comparing the graphite morphology to a shape for which theoretical stress concentrations have been determined. Studies have been done to this effect for gray and nodular irons<sup>(5-7)</sup>. In this



thesis the effect that graphite nodules have on the mechanical properties of pearlitic malleable iron are characterized by determining the matrix properties and the stress concentrations, from the graphite, with direct strain measurements.



## CHAPTER 2

### MATERIAL

Malleable iron is cast as a white iron. It is then heated into the austenite plus carbide region and held at this temperature until the large carbides have converted into graphite nodules. From this point the rate of cooling and subsequent heat treatments are dependent on the desired matrix structure<sup>(8,9)</sup>.

Specimens used in this program were cast and machined by General Motors Central Foundry. After the specimens were cast they were heated to more than 1700°F for 12 hours. The specimens were then oil quenched to 150°F. Finally they were tempered at approximately 1200°F and held at this temperature for the time necessary to produce the desired hardness.

Specimens were received in hardness groups as tested by General Motors. They came in seven hardness lots according to the following Brinell hardness diameters, 3.8; 3.9; 4.0; 4.2; 4.3; 4.6; 4.7 mm. Due to the similarity of properties between the close hardness ranges, the specimens were regrouped into four hardness lots. The corresponding average Brinell hardness numbers were found for each Brinell hardness diameter range<sup>(10)</sup>. BHN values will be used for this thesis. Hardness ranges and the number of specimens tested in each range are listed in Table 1.





Table 1. Specimens tested

BHD (mm)	BHN	HV (matrix)	Specimens Tested
3.8-3.9	250	372	17
4.0	230	336	19
4.2-4.3	200	327	17
4.6-4.7	170	294	20

The Vickers microhardness of the matrix was measured for each specimen. Table 1 has the average Vickers hardness for each range. Data presented in this thesis are grouped according to Brinell hardnesses. When the specimens were regrouped according to Vickers hardness values the results became more scattered.

An etched and unetched microstructure of each hardness lot is shown in Figure 1. Unetched microstructures illustrate the morphology of the graphite nodules. There is little difference between the nodule morphology of each hardness range. Nodules are compact and show only slight alignment. Both of these characteristics improve the mechanical properties.

Etched microstructures show the matrix to be martinsite, not pearlite, as it's name suggests. There is also little difference between the etched microstructures, but this is expected since the only difference between these hardness lots is due to the degree of tempering.



The surface of the specimens used for the strain-life tests were machined. The effect machining has on the surface of this material is shown in Figure 2. Cracking around the nodule is caused by machining. A second feature found in the surface of many of these specimens was microshrinkage. Figure 3 shows a common looking shrinkage. Many of the shrinkages had this type of circular symmetry, but not all.



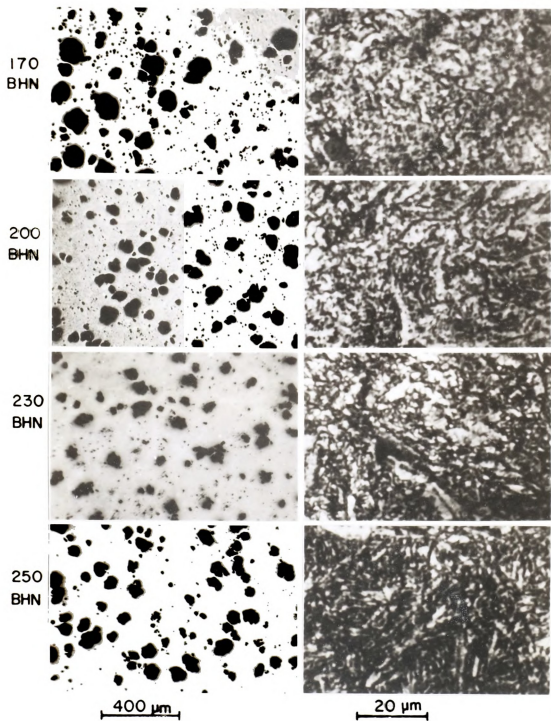


Figure 1. Etched and unetched microstructures



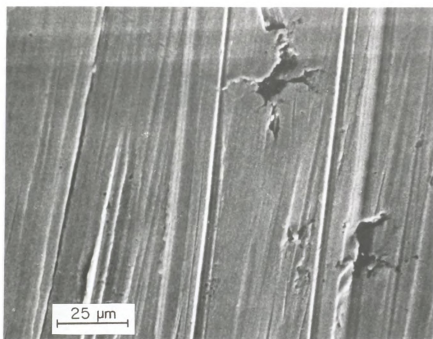


Figure 2. Machined test surface

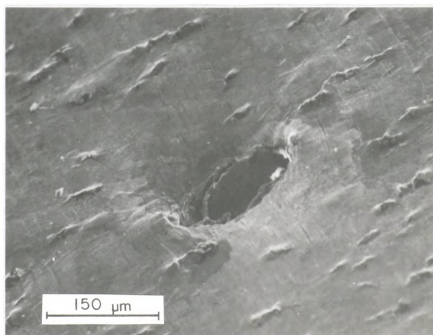


Figure 3. Microshrinkage



### CHAPTER 3

#### STRAIN-LIFE TESTS

##### 3.1 PROCEDURE

Standard strain-Life procedures were used<sup>(11)</sup> to produce the strain-life data. Data were produced from strain controlled axial fatigue tests. An MTS closed loop, servo-hydraulic fatigue system was used<sup>(12)</sup>. Strain was induced into the specimen in the form of a constant amplitude, fully reversed, sine wave, shown in Figure 4. Each specimen was tested to failure or no less than  $10^6$  cycles. Stress-strain hysteresis loops were recorded at convenient increments for data reduction purposes.

The specimen configuration is given in Figure 5. This large test section was used to help homogenize the effects of the nearly macroscopic discontinuities and to utilize an available casting mold.

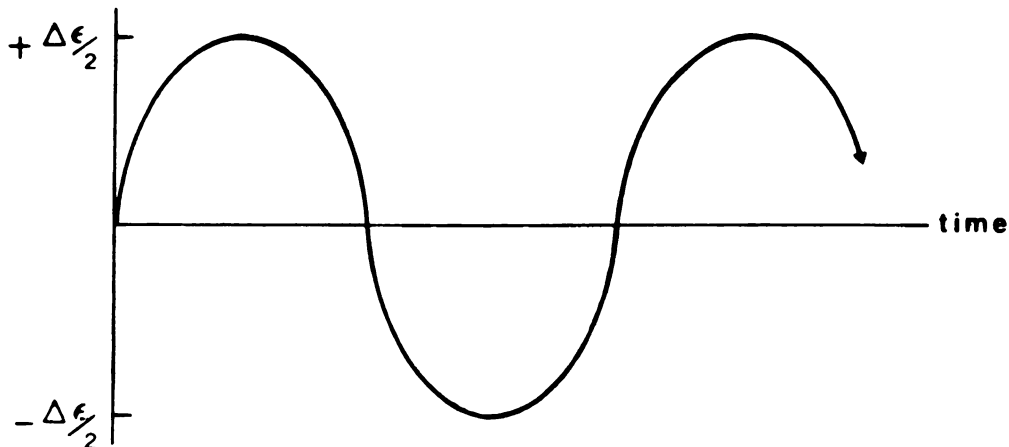


Figure 4. Strain/time sine wave

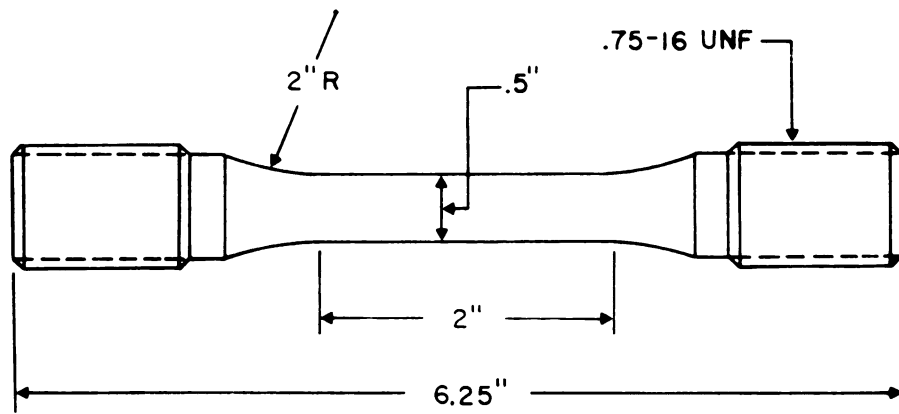


Figure 5. Specimen schematic

### 3.2 OBSERVATIONS

Test frequencies from .1 to 20 Hz were used. Low frequencies were necessary to prevent the large strain amplitude test specimens from overheating. The use of test frequencies of more than 20 Hz was inhibited by the loss of control caused by the large test section.

Failures produced a classic fatigue fracture as seen in Figure 6. The well defined line between the fatigue and brittle fracture regions was observed in many of the specimens. Many of the surfaces could not be classified due to the compression of the surfaces by the hydraulic ram after shut down. In all but one of the preserved fracture surfaces, a fatigue failure could be identified by a fatigue crack growth region. Approximately 40% of the failures, which could be examined, initiated at shrinkages. Several of the shrinkages that initiated failure were located by macroscopic inspection before testing. All



failures initiated at the surface. This may be attributed to the surface degradation produced by machining.



Figure 6. Failure surface



### 3.3 DATA

Strain-life data are measured from stress-strain hysteresis loops. The parameters which are derived from a hysteresis loop are shown in Figure 7. Compressive and tensile moduli of elasticity ( $E_c$  and  $E_t$ ) are both measured because they are not the same for most cast irons. Stress amplitudes ( $\Delta\sigma/2$ ) and total strain amplitudes ( $\Delta\epsilon/2$ ) are measured from the hysteresis peaks. Elastic strain ( $\Delta\epsilon_e/2$ ) is determined by dividing the stress amplitude by the average modulus of elasticity.

$$\Delta\epsilon_e/2 = (\Delta\sigma/2) / ((E_t + E_c)/2) = \Delta\sigma / (E_t + E_c) \quad (\text{Equation 1})$$

Total strain is the sum of the elastic and plastic strains ( $\Delta\epsilon_p/2$ ). Therefore, plastic strain is calculated as the difference between the total and the elastic strains.

$$\Delta\epsilon_p/2 = \Delta\epsilon/2 - \Delta\epsilon_e/2 \quad (\text{Equation 2})$$

As mentioned, the strain amplitude is held constant for strain-life testing. The stress amplitude will often change during a test. This material generally had a decreasing stress amplitude (cyclically softened) as it was cycled. Most of the change occurs early in the life of these specimens. Hysteresis loops recorded,

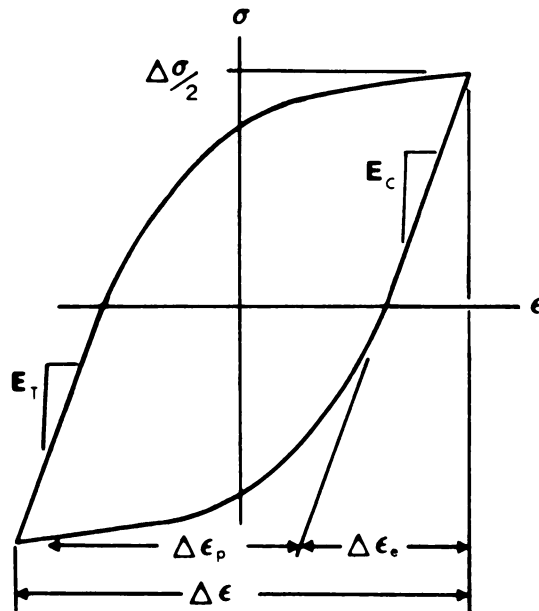


Figure 7. Schematic of a hysteresis loop with parameters

between one half of cycles to failure to near failure were considered stable for this material. The difference between the first hysteresis and the stable hysteresis for each hardness group tested, at  $\pm 3\%$   $\epsilon$  can be seen in Figures 8 and 9. The 250 BHN group showed an average decrease in stress amplitude of 12%, while the 170 BHN group had an average increase in stress amplitude of 4%. Approximately half of the specimens in the 170 BHN group cyclically hardened and half cyclically softened. Stable loops were used to calculate the data in Table 2. Included in the Table are the reversals to failure, (two times the cycles,  $2N_f$ ) for each specimen.





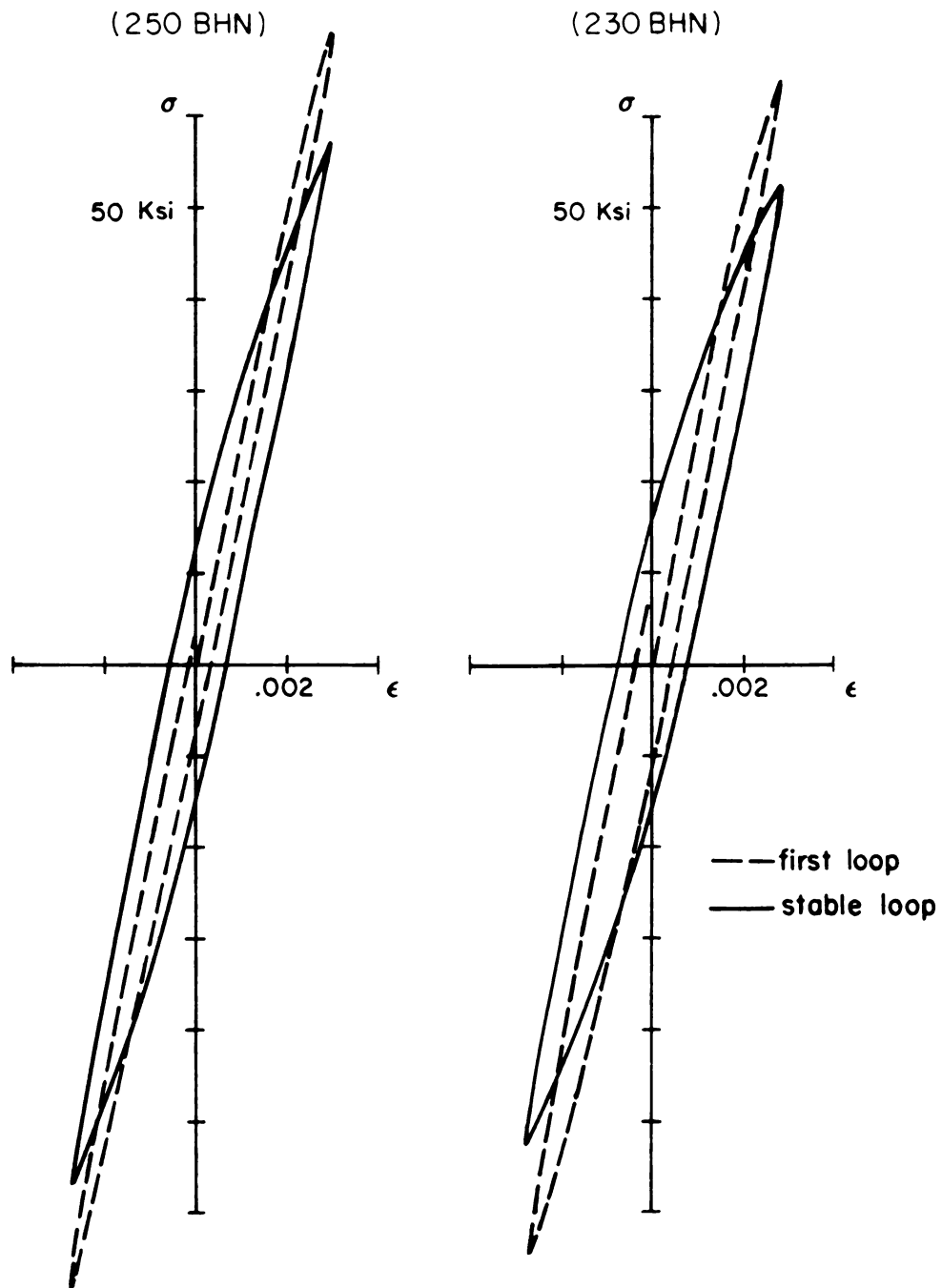


Figure 8. Hysteresis loops from 250 and 230 BHN specimen

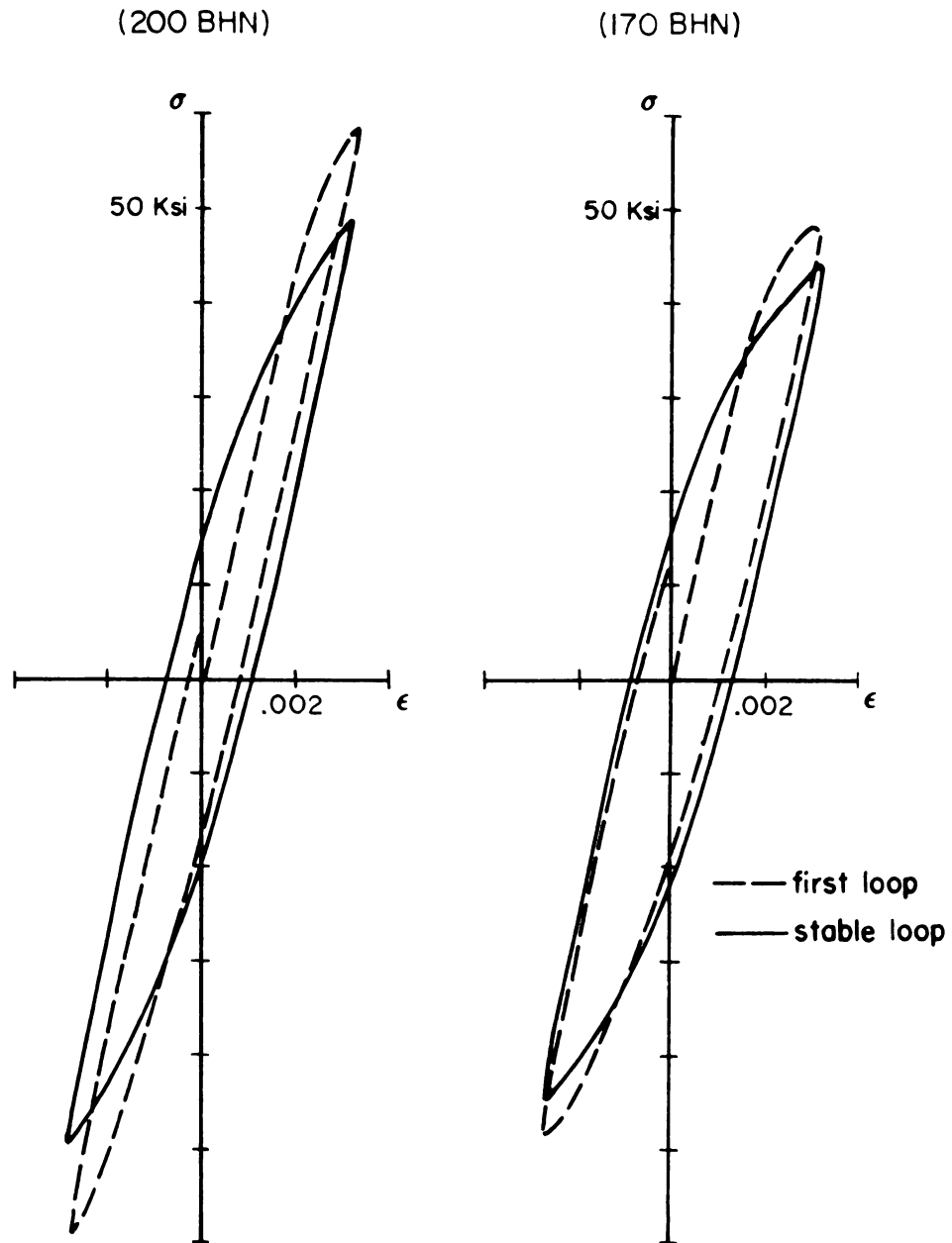


Figure 9. Hysteresis loops from 200 and 170 BHN specimen

Table 2. Strain-life data

$E_t$	$E_c$	$\Delta\sigma/2$	$\Delta\epsilon/2$	$\Delta\epsilon_e/2$	$\Delta\epsilon_p/2$	$2N_f$
(10 <sup>6</sup> Psi)	(10 <sup>6</sup> Psi)	(Ksi)				
<hr/> 250 BHN <hr/>						
25.0	22.2	78.2	.00982	.00331	.00651	178
24.5	22.0	78.2	.00980	.00337	.00653	174
25.0	23.0	72.0	.00782	.00300	.00482	254
26.8	23.2	75.0	.00781	.00300	.00481	202
24.8	23.8	62.3	.00485	.00257	.00220	1780
25.2	22.2	62.6	.00484	.00264	.00220	1300
26.2	24.0	56.4	.00284	.00225	.00059	16900
25.5	24.5	55.4	.00284	.00222	.00062	11500
27.0	26.6	49.6	.00193	.00185	.00008	97200
27.2	26.5	48.8	.00193	.00182	.00011	172800
27.2	27.2	42.1	.00160	.00154	.00006	362000
27.0	27.0	41.8	.00157	.00157	.00000	618000
26.5	26.5	40.5	.00153	.00153	.00000	356000
26.5	26.5	39.3	.00148	.00148	.00000	404000
27.5	27.5	39.2	.00143	.00143	.00000	810000
27.2	27.2	38.6	.00142	.00142	.00000	8714000
<hr/> 230 BHN <hr/>						
24.0	23.0	76.5	.00976	.00326	.00650	100
23.5	22.5	71.8	.00782	.00312	.00470	170
26.0	23.5	67.9	.00644	.00274	.00370	324
25.2	23.9	63.2	.00484	.00258	.00226	2490
25.4	23.8	64.6	.00482	.00263	.00219	2090
25.2	25.0	58.6	.00359	.00233	.00126	6480
24.0	24.8	52.0	.00286	.00213	.00073	11100
26.2	25.0	50.8	.00229	.00198	.00031	30200
25.1	25.2	49.5	.00206	.00197	.00009	73400
26.8	25.8	47.8	.00188	.00181	.00007	182000
26.2	26.2	47.2	.00187	.00180	.00007	194000
26.5	26.5	47.4	.00187	.00179	.00008	111000
27.5	27.5	48.0	.00183	.00174	.00009	144000
26.0	26.0	46.1	.00180	.00177	.00003	131000
26.8	26.8	43.0	.00161	.00161	.00000	295000
25.8	25.8	41.2	.00160	.00160	.00000	706000
26.8	26.8	38.5	.00144	.00144	.00000	1620000
27.0	27.0	38.0	.00141	.00141	.00000	431000

Table 2. continued

200 BHN						
26.2	22.8	67.7	.00983	.00276	.00707	156
24.5	22.2	67.7	.00982	.00290	.00692	88
22.5	22.2	62.1	.00783	.00278	.00505	346
25.2	23.0	62.5	.00780	.00259	.00521	380
22.8	22.2	56.5	.00587	.00251	.00336	686
24.8	22.8	60.8	.00551	.00256	.00295	1320
23.5	21.8	56.7	.00506	.00251	.00255	2120
23.2	19.9	56.8	.00503	.00263	.00240	3320
24.5	23.8	50.8	.00385	.00211	.00174	1950
25.5	25.0	52.0	.00380	.00206	.00174	830
23.8	23.8	49.5	.00300	.00208	.00092	9120
23.2	22.8	48.5	.00291	.00211	.00080	11000
27.0	26.2	45.5	.00191	.00171	.00020	73200
27.0	25.8	44.2	.00190	.00168	.00022	59400
29.0	27.2	43.8	.00163	.00155	.00008	87800
25.2	25.2	39.0	.00160	.00154	.00006	176000
25.2	25.2	39.9	.00157	.00157	.00000	538000
25.8	25.8	37.0	.00143	.00143	.00000	438000
26.2	26.2	37.2	.00142	.00140	.00002	357000
26.0	26.0	33.1	.00127	.00127	.00000	610000
170 BHN						
21.0	20.5	50.3	.00798	.00242	.00556	92
23.5	21.0	49.7	.00592	.00219	.00373	268
24.2	22.4	49.5	.00490	.00220	.00270	600
22.5	21.5	49.5	.00442	.00224	.00218	1080
24.5	23.2	47.0	.00390	.00197	.00193	1560
24.2	23.7	46.7	.00353	.00195	.00158	4170
22.9	22.0	40.8	.00323	.00182	.00141	706
23.8	23.0	44.2	.00295	.00189	.00106	5700
23.5	23.5	42.2	.00270	.00180	.00090	3290
23.8	23.8	43.8	.00250	.00184	.00066	18200
24.2	24.0	43.8	.00242	.00182	.00060	16800
25.8	24.8	45.2	.00193	.00179	.00014	51600
25.8	24.8	39.0	.00175	.00154	.00021	60000
23.8	23.6	35.3	.00160	.00149	.00011	64600
25.2	25.2	33.1	.00134	.00131	.00003	263000
23.5	23.5	28.5	.00126	.00121	.00005	850000
24.5	24.5	29.6	.00121	.00121	.00000	1140000
25.5	25.5	30.3	.00119	.00119	.00000	937000
24.0	24.0	26.7	.00111	.00111	.00000	1200000

### 3.4 RESULTS

A cyclic stress-strain curve is produced by connecting the tips of stabilized hysteresis loops. The stress and plastic strain from the cyclic stress-strain curve are linearly related on a log-log scale, illustrated in Figure 10. The relationship can be written as:

$$\Delta\sigma/2 = K' (\Delta\epsilon_p/2)^{n'} \quad (\text{Equation 3})$$

The cyclic strain hardening exponent ( $n'$ ) and the cyclic strength coefficient ( $K'$ ) are determined by using the least squares method on the logarithmic values of stress and plastic strain.

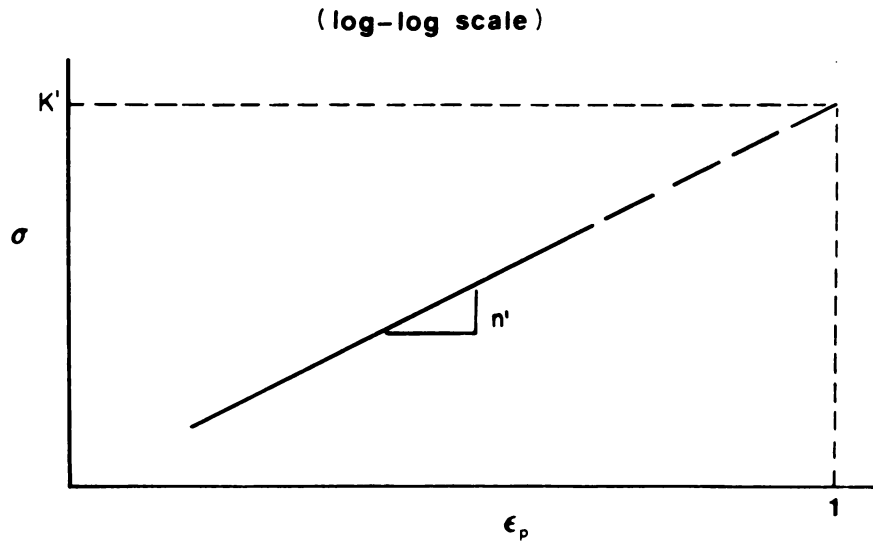


Figure 10. Log-stress/log-plastic strain schematic



Cyclic stress-strain curves for each hardness group are given in Figure 11. The cyclic response of this material exhibits less change, with respect to hardness, than the monotonic response. The cyclic yield stress varied from 35 to 50 Ksi while the monotonic yield varied from 30 to 70 Ksi. The difference between the maximum and minimum monotonic yield stresses is 2.5 times greater than the difference between the cyclic yield stresses.

The change in cyclic properties did exhibit trends with respect to hardness. The average elastic modulus for each group varied from  $24 \cdot 10^6$  Psi to  $25.5 \cdot 10^6$  Psi, with increasing hardness. Also the cyclic strain hardening exponents and the cyclic strength coefficient increased with increasing hardness. This can be seen in Figure 12 which has the log-stress versus log-plastic strain lines for each hardness group.





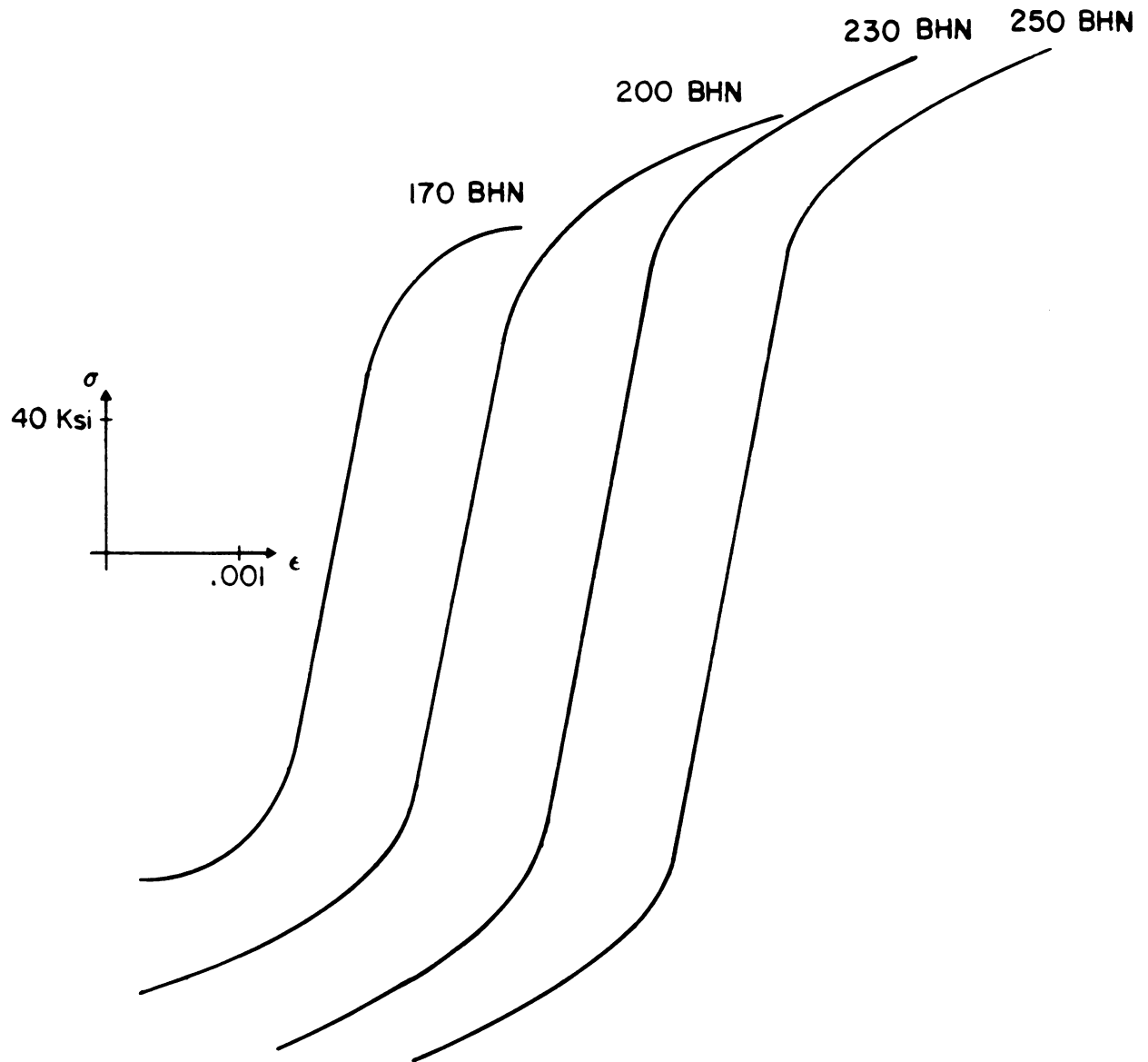


Figure 11. Cyclic stress-strain curves



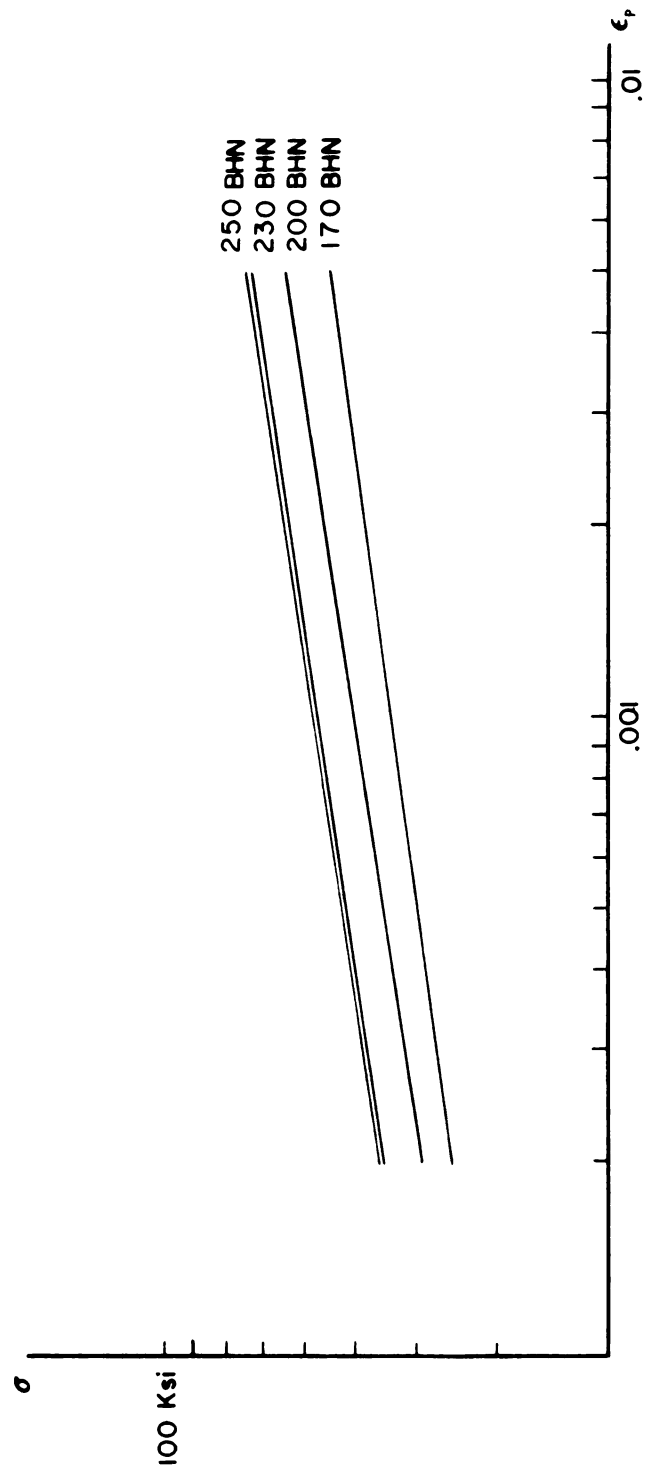


Figure 12. Log-stress/log-plastic strain lines



Relationships have been made between strain and reversals to failure. These are illustrated in Figure 13, where total strain, plastic strain, and elastic strain are each plotted against reversals to failure, on a log-log scale. Elastic and plastic strains both have linear relationships on this scale.

$$\Delta\epsilon_p/2 = \epsilon'_f(2N_f)^c \quad (\text{Equation 4})$$

$$\Delta\epsilon_e/2 = (\sigma'_f/E)(2N_f)^b \quad (\text{Equation 5})$$

The total strain is therefore:

$$\Delta\epsilon/2 = (\sigma'_f/E)(2N_f)^b + \epsilon'_f(2N_f)^c \quad (\text{Equation 6})$$

The last parameter to be produced from the strain-life curve is the transition fatigue life ( $2N_t$ ). This is the point where the elastic and plastic strains are equal, and is determined by equating Equations 4 and 5. The solution is:

$$2N_t = (\epsilon'_f \cdot E / \sigma'_f)^{1/(b-c)} \quad (\text{equation 7})$$

The stain-life curves for each test group are given in Figures 14 through 17. Each plot contains the total strain, plastic strain and elastic strain curves, with data points. Stress-strain data were measured from the stable hysteresis loops as described in the data

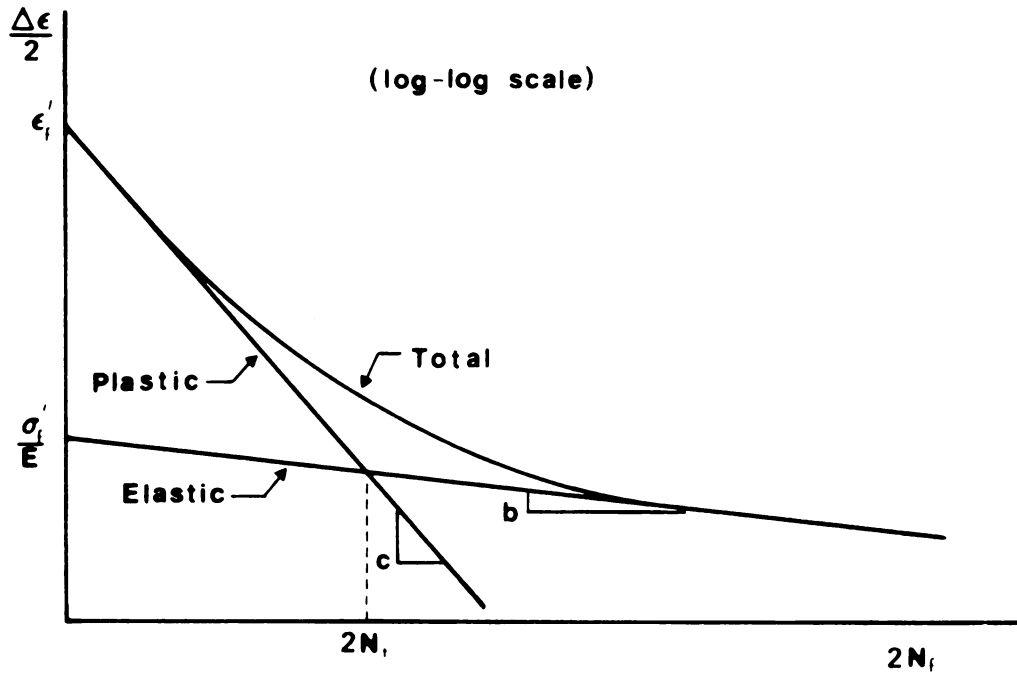


Figure 13. Schematic of strain-life curve with parameters

section. Logarithmic values of plastic strain, elastic strain, and reversals to failure were used in a least squares formulation to produce the elastic and plastic lines. The total strain curves were determined by summing the elastic and plastic strain values as indicated in Equation 6.

The fatigue ductility coefficient ( $\epsilon'_f$ ), fatigue strength coefficient ( $\sigma'_f$ ), fatigue ductility exponent ( $c$ ) and fatigue strength exponent ( $b$ ) were calculated from the strain-life lines that were determined with the least squares method. The transition fatigue life was found with Equation 7. Values of these parameters are listed in Table 3, along with the cyclic strain hardening exponents and the



cyclic strength coefficients.

Figure 18 has the total strain curves for each test lot. There is a small difference between these curves. Lower hardness groups failed at slightly shorter lives than the harder groups. The elastic strain lines in Figure 19, exhibit a similar trend. The Plastic strain lines given in Figure 20 have the least spread.

Points on the strain-life plots exhibit a small degree of scattering, considering this material is a cast iron. The largest scatter is observed in the lower hardness groups. Specimens which failed far before their expected lives did not exhibit unusual voids or inclusions, but they often had low first cycle yield stresses. Although specimens tested with the low first cycle yield stresses generally cyclically hardened to a cyclic stress-strain response similar to other specimens in their hardness range, the life of these specimens was usually much shorter. The large difference in monotonic stress-strain behavior within a hardness range indicates that the Brinell hardness test does not accurately predict the initial condition of this material<sup>(13)</sup>. Another source of scatter is due to some specimens being put through more tempering cycles than other specimens in the same hardness range.

The 170 BHN material showed the most scatter, with one failure close to an order of magnitude shorter than expected. More scattering might be expected from this group since many of the specimens were cast from different lots on different days.





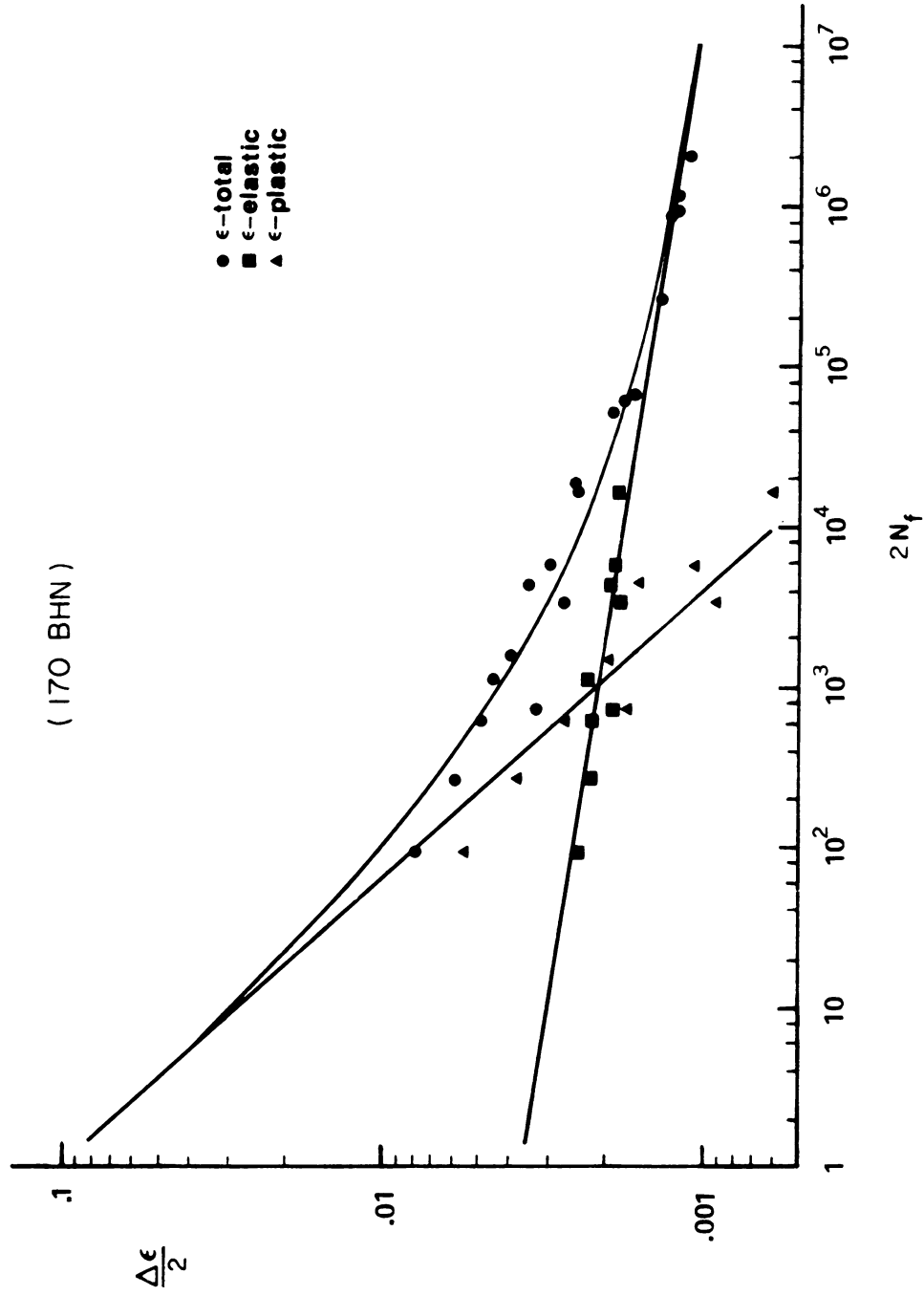


Figure 14. Strain-life curve for 170 BHN specimens



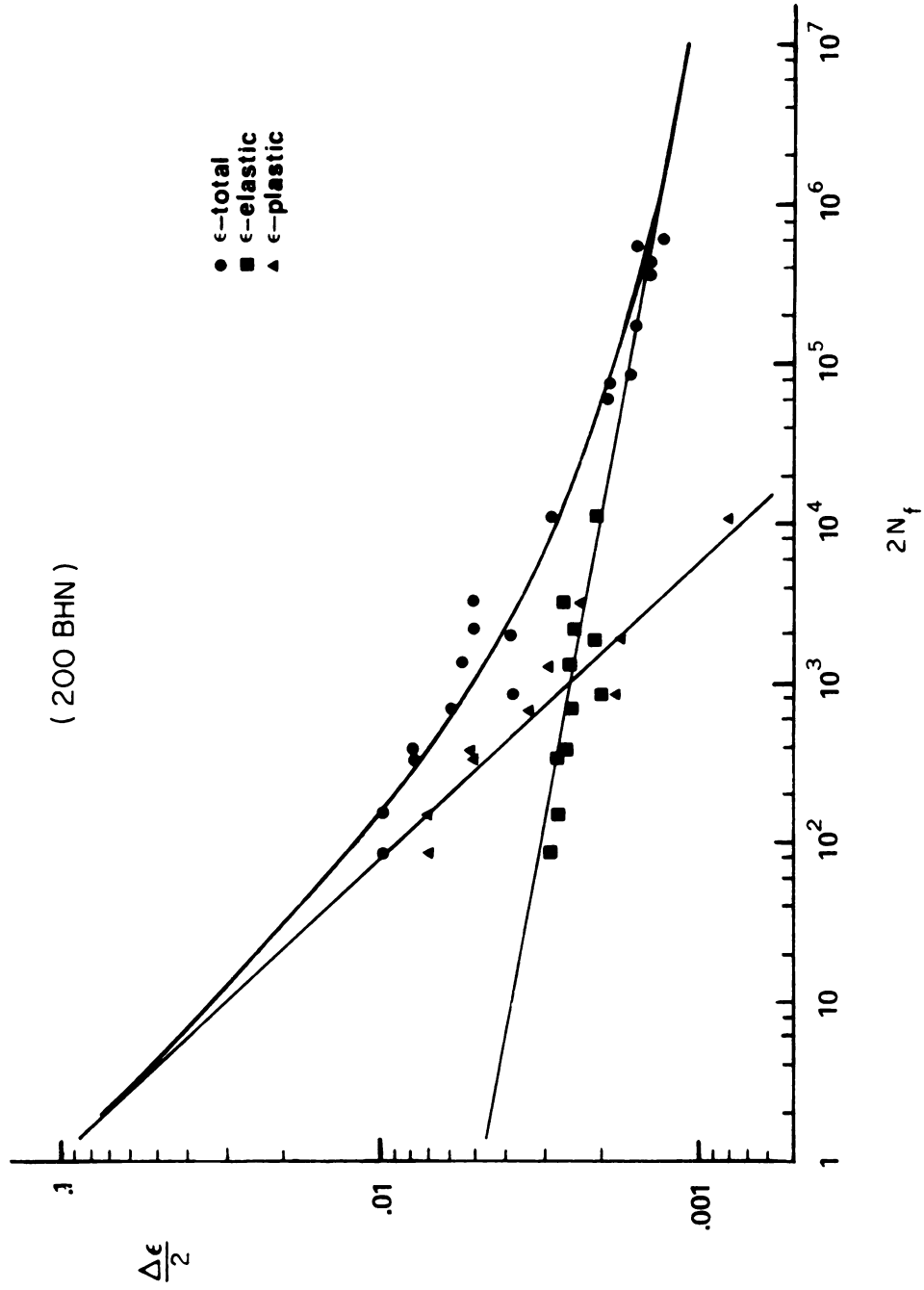


Figure 15. Strain-life curve for 200 BHN specimens

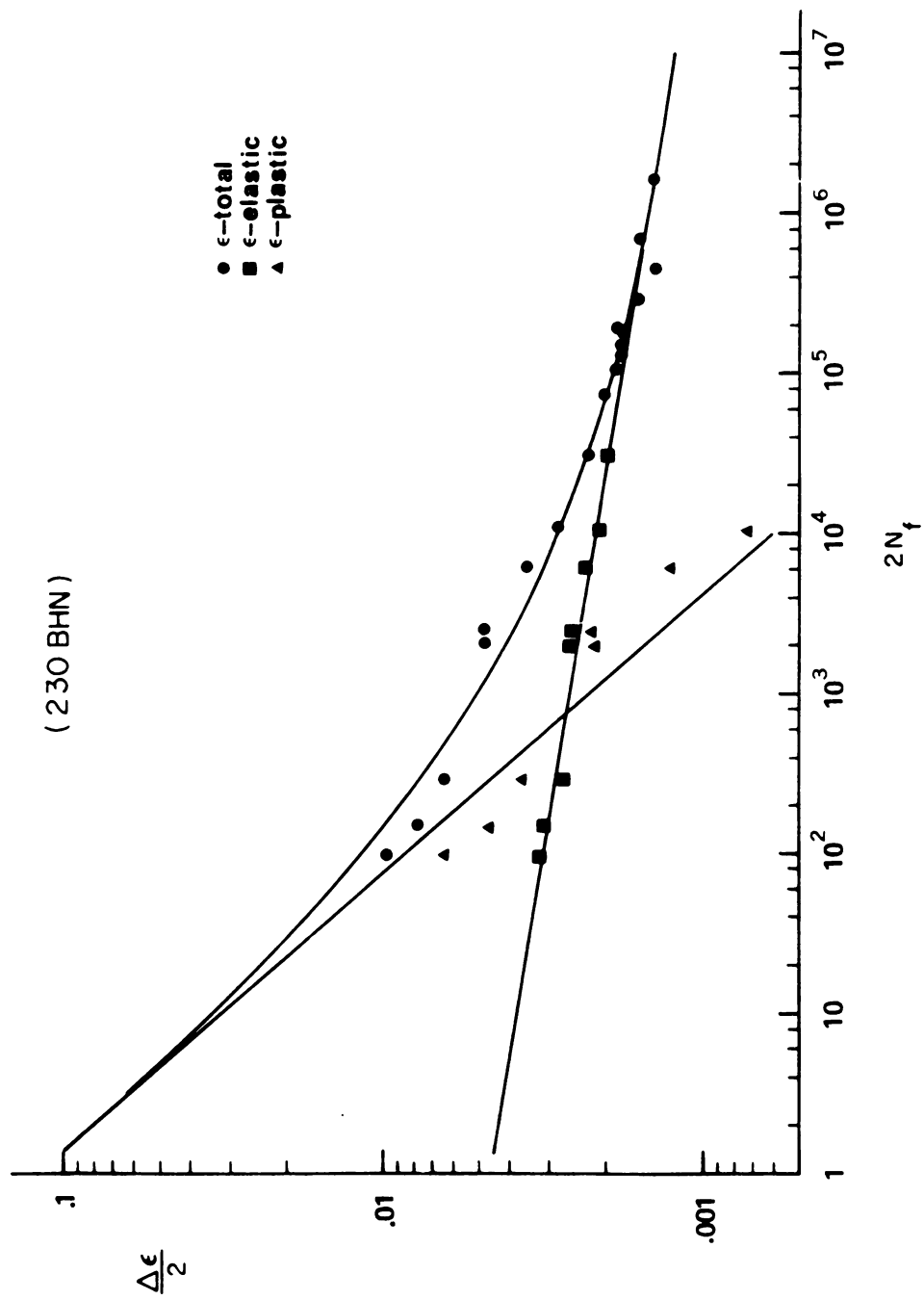


Figure 16. Strain-life curves for 230 BHN specimens



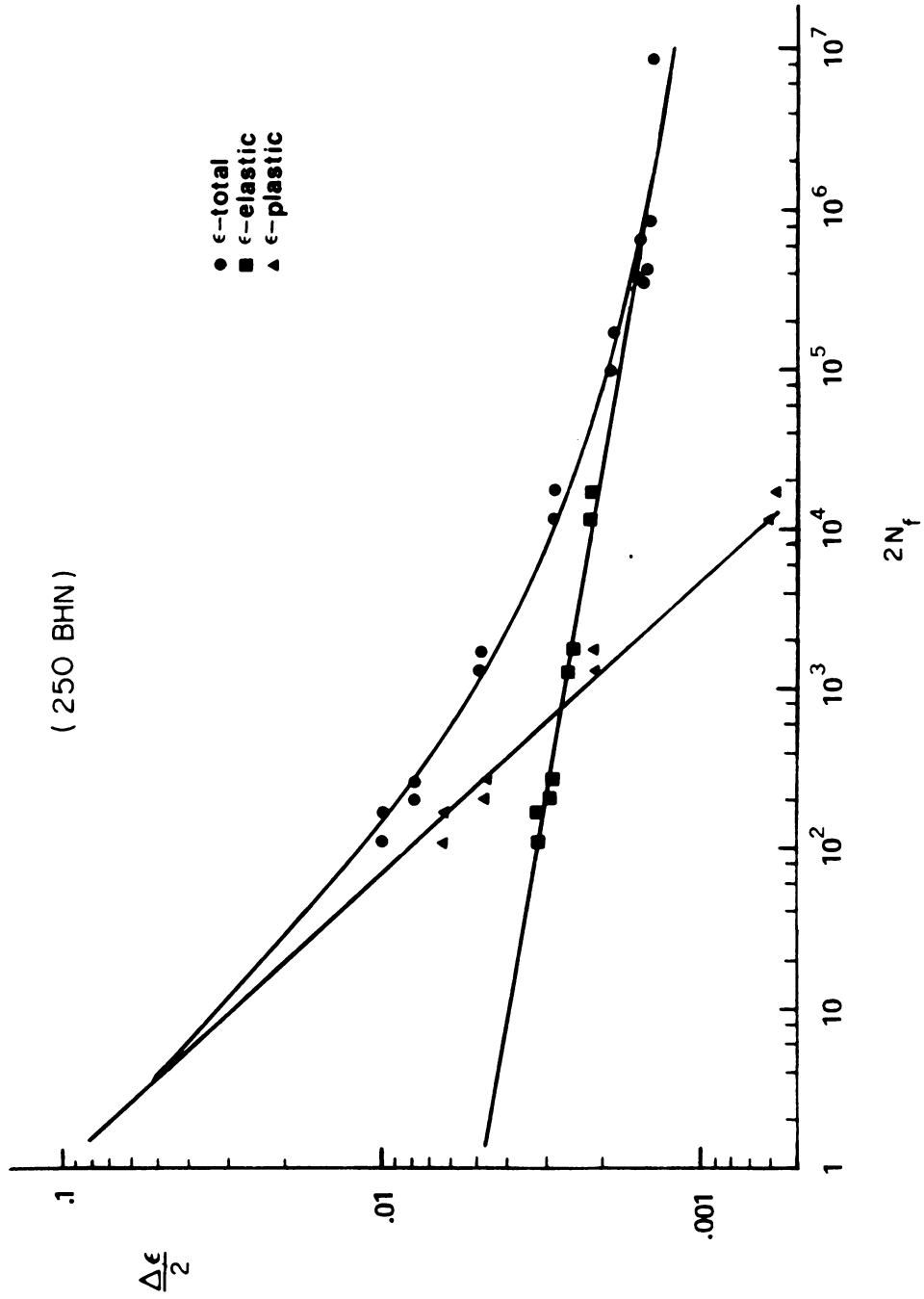


Figure 17. Strain-life curves for 250 BHN specimens





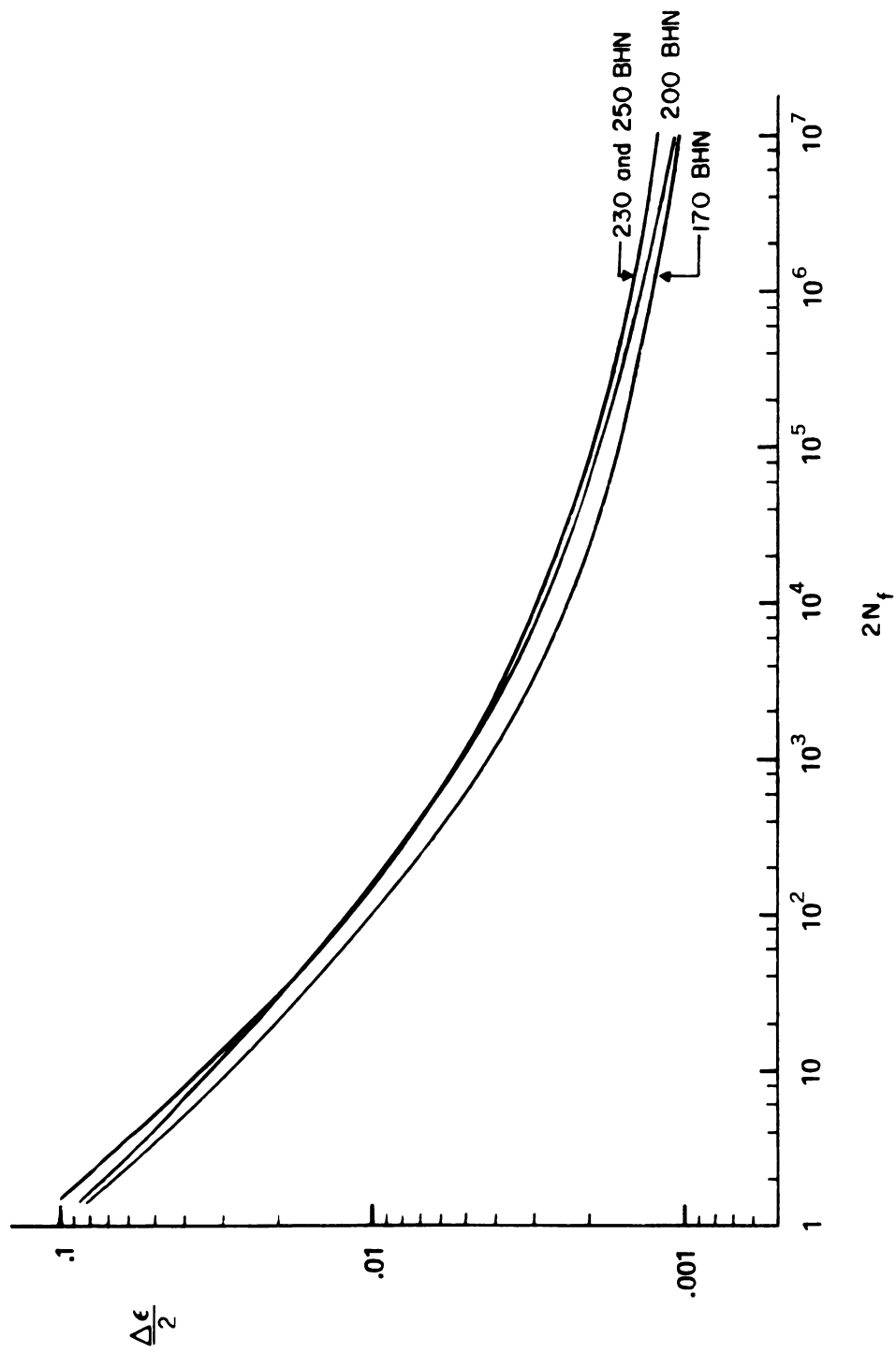


Figure 18. Total strain-life curves



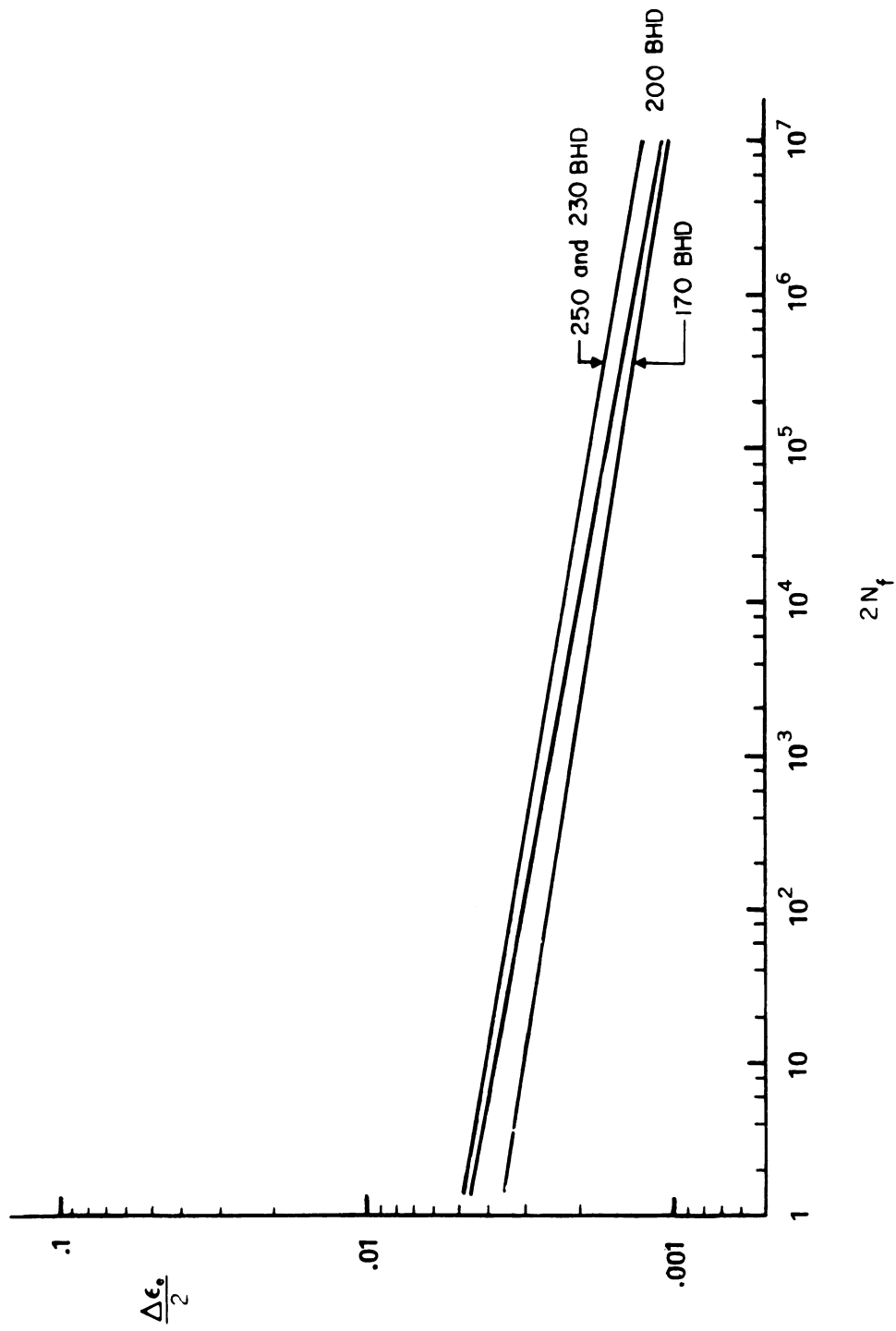


Figure 19. Elastic strain-life lines



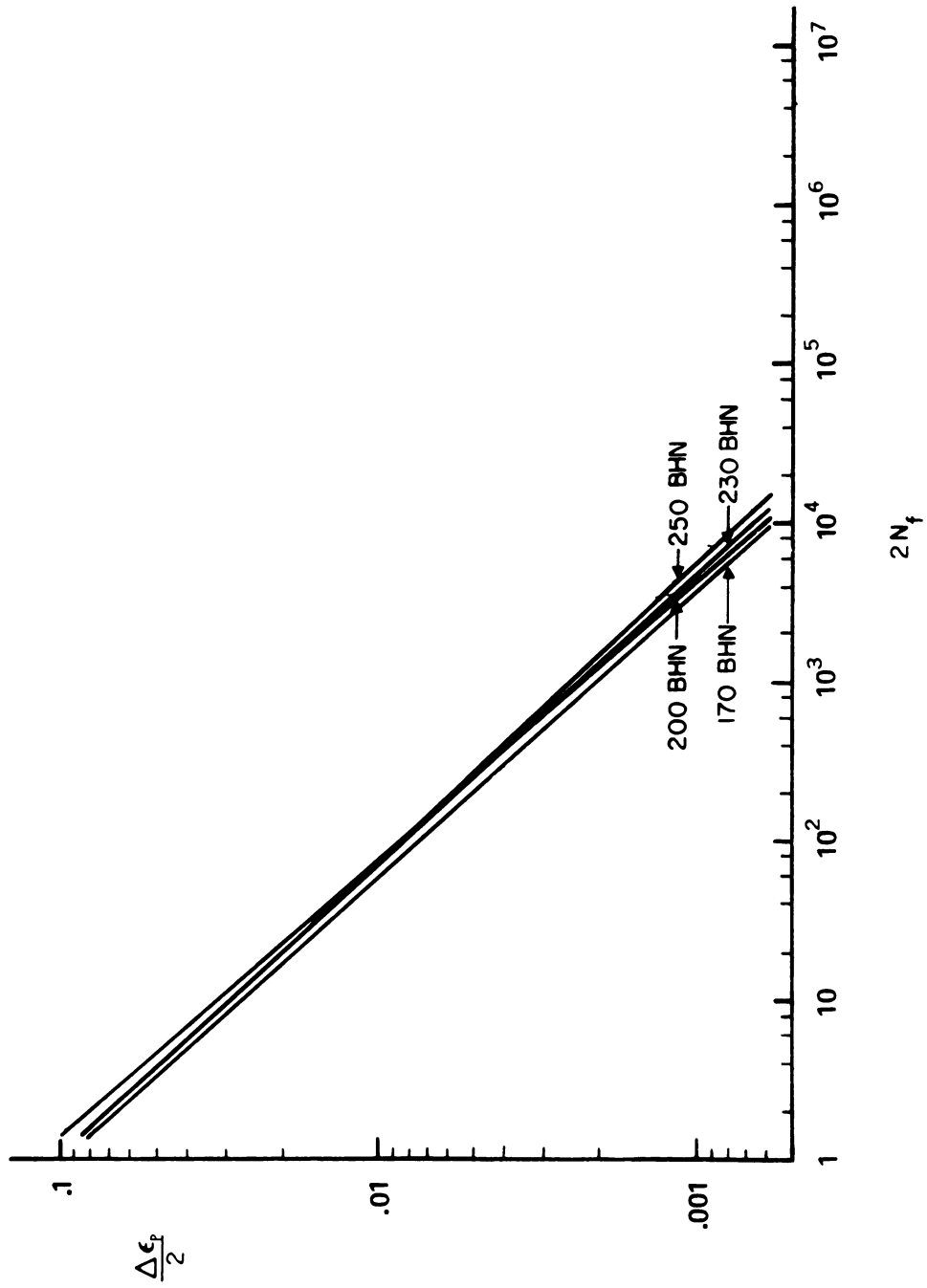


Figure 20. Plastic strain-life lines

Table 3. Strain-life properties

Property	Hardness groups (BHN)			
	170	200	230	250
$n'$	.14	.15	.15	.15
$K'$ (Ksi)	150	200	220	230
$b$	-.079	-.091	-.084	-.086
$c$	-.56	-.54	-.57	-.55
$\sigma'_f$ (Ksi)	90	115	115	120
$\epsilon'_f$	.100	.100	.140	.140
$2N_t$	975	1010	755	690



## CHAPTER 4

### ANALYSIS OF STRESS CONCENTRATIONS

Nueber's rule<sup>(14)</sup> is applied to determine stress concentration factors based on strain measurements taken in the matrix and around discontinuities.

#### 4.1 TEST PROCEDURE

An interferometric strain gage (ISG) was used to measure strains over short gage lengths in both remote and critical regions. This system monitors interference patterns formed by the reflection of coherent light from two Vickers microhardness indentations. The distance between the fringes is inversely proportional to the distance between the indentations. Therefore, the fractional change in distance between the fringes is a measure of strain between the indentations. Detailed explanations of the system have been published<sup>(15,16)</sup>.

Five tests were run. One to check the calibration of the ISG and four to obtain data. From these four tests two were run on 170 BHN specimens and two on 250 BHN specimens. These tests were also run under constant amplitude, sine wave, strain control. Both hardness groups were tested at two strain ranges,  $\pm 0.3\%$   $\epsilon$  and  $\pm 0.14\%$   $\epsilon$ . The strain monitored to control these tests came from an extensometer. Each specimen was cycled until a crack (macroscopically visible) was produced. A copy, of a series of hysteresis loops recorded from ISG





measurements, taken from indentations around a nodule is given in Figure 21.

Gage lengths from 75 to 180  $\mu\text{m}$  were used for strain measurements. These strains were measured around nodules, near shrinkages, and in the matrix away from the discontinuities. One example of each is shown in figure 22.

The position of the indentations around nodules was varied to find locations with large strain concentrations. Because some shrinkages were close to 300  $\mu\text{m}$  in diameter, indentations could be put closer to the notch root. Six sets of indentations and respective discontinuity, are shown in Figure 23. These are micrographs of replicas made from test locations.

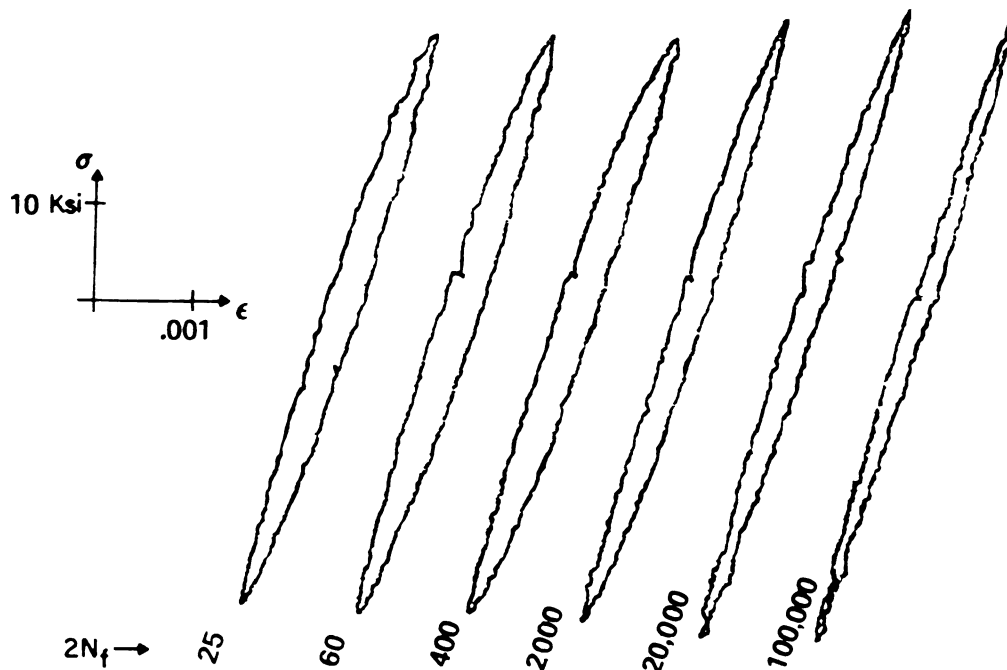
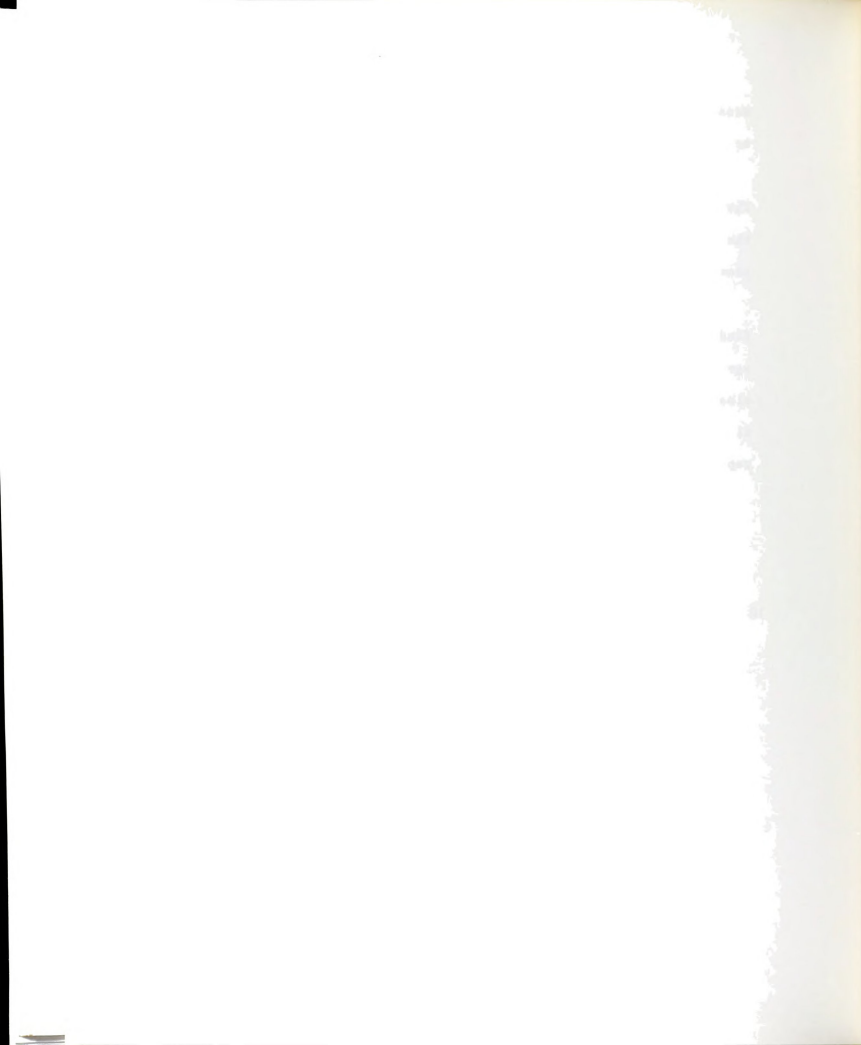


Figure 21. Hysteresis loops recorded from interferometric strain measurements



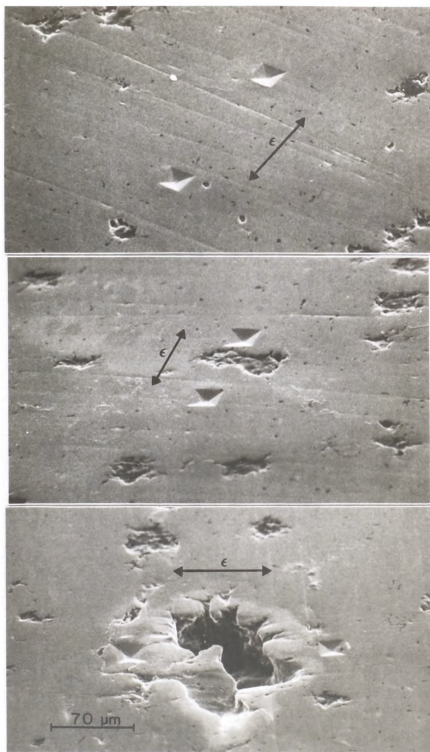


Figure 22. Test regions with indentations



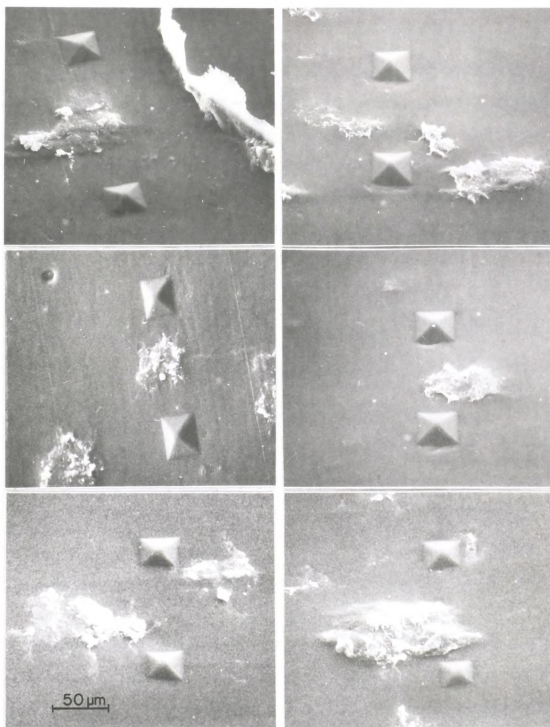


Figure 23. Replicas of discontinuities with indentations

#### 4.2 Remote and Local Behavior

In general, stress concentrations are determined by comparing a defined remote response to a local response at the most highly stressed regions of a material. The location of remote and local regions is illustrated in Figure 24. In the following analysis the remote response is the response of the matrix away from discontinuities and the local response is measured near the discontinuities.

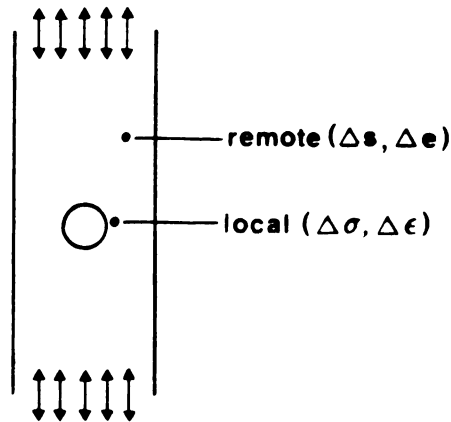


Figure 24. Schematic of remote and local regions.

Characterization of the matrix properties of a cast iron have been done by comparing the structure and hardness of the matrix to a cast steel with a similar structure and hardness. Matrix properties will be determined here by direct strain measurements and corrected stress measurements.

Stresses recorded during these tests were determined by dividing

the measured load by the crosssectional area of the specimen. It is assumed that the matrix supports the entire load. Therefore the stress in the matrix was calculated by dividing the load, by the crosssectional area of the specimen minus the crosssectional area of the nodules. The area of the nodules was measured from a micrograph.

Data obtained from the stress-strain response of the matrix are listed in Table 4. Corrected stress values are included.

Table 4. Matrix hysteresis data

	170 BHN Specimens		250 BHN Specimens	
$\Delta\epsilon/2$ (extensometer)	.0014	.0030	.0014	.0030
E ( $10^6$ Psi)	27	27	29	28
$\Delta\sigma/2$ (Ksi)	33	46	34	49
$\Delta\sigma/2$ (corrected)	38	53	39	57
$\Delta\epsilon/2$	.00126	.00265	.00117	.00215
$\Delta\epsilon_e/2$	.00118	.00169	.00115	.00177
$\Delta\epsilon_p/2$	.00008	.00096	.00002	.00038

In section 3.4, a method for determining cyclic stress-strain curves was described. That method is not used here because there are only two sets of points to be used in a least squares calculation. Instead, the cyclic stress-strain curves in Figure 25 were derived from the stable hysteresis loops recorded from the matrix. The portion of the hysteresis loop from the compressive peak, clockwise, to the tensile peak was used. One half of the stress and strain values



measured from these curves were replotted to produce the cyclic stress-strain curves.

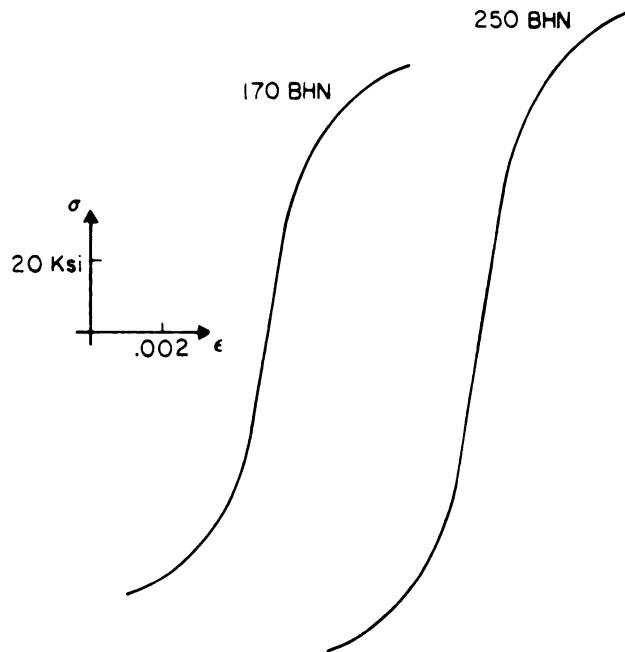


Figure 25. Cyclic stress/strain curves from the matrix

As mentioned, there is a linear relation between the log-stress and log-plastic strain values from cyclic stress-strain curves. An equation for plastic strain can be produced by rearranging Equation 3.

$$\Delta \epsilon_p / 2 = (\Delta \sigma / 2K')^{1/n'} \quad (\text{Equation 8})$$

The total strain can be written as the sum of the elastic and plastic strains.



$$\Delta\epsilon/2 = \Delta\epsilon_e/2 + \Delta\epsilon_p/2 = \Delta\sigma/2E + (\Delta\sigma/2K')^{1/n'} \quad (\text{Equation 9})$$

The cyclic strain hardening exponent and the cyclic strength coefficient were again calculated using the least squares method. The values of these parameters, for both hardness groups, are listed in table 5.

Table 5. Cyclic stress-strain parameters for the matrix

	170 BHN	250 BHN
K'	187	213
n'	.18	.17

Fourteen local regions were monitored in the  $\pm 1.4\%$   $\epsilon$  tests. Strain amplitudes recorded from these regions are given in the next section. Data from the  $\pm 3\%$   $\epsilon$  tests are not included because crack growth was observed throughout the test life of these specimens and this study is only concerned with a continuum approach for determining stress concentration factors. Because of crack growth, the strain readings from the  $\pm 3\%$   $\epsilon$  tests were largely a measure of crack opening and closure. The number of crack sites and the extent of crack growth is illustrated in Figure 26.

In each test the strains measured in the matrix were less than the strains measured from the extensometer, and strains measured across discontinuities were larger than both. A copy of a hysteresis loop recorded from each location is given in Figure 27.

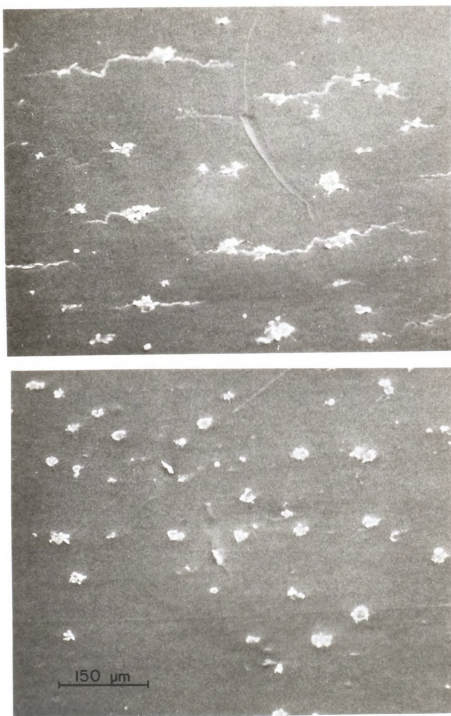


Figure 26. Micrographs of replicas from specimens tested at  $\pm 0.3\% \epsilon$  and  $\pm 0.14\% \epsilon$

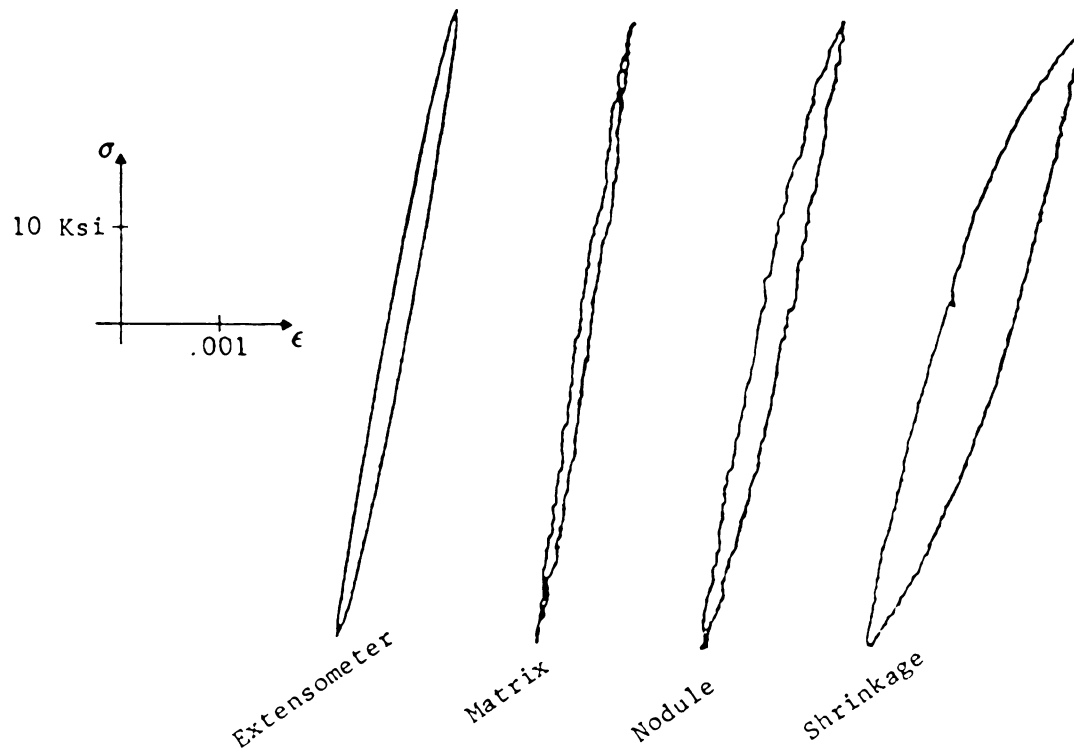


Figure 27. Hysteresis loops recorded near 1000 cycles



#### 4.3 NUEBER APPLICATION

Nueber's rule has been applied to fatigue studies of notched materials. This rule accounts for the effect of plastic deformation in notched members. The stress concentration factor is related to the remote and local stresses and strains. The relationship between these parameters is given in this equation.

$$K_t = [(\Delta\sigma \cdot \Delta\epsilon) / (\Delta S \cdot \Delta e)]^{1/2} \quad (\text{Equation 10})$$

The application of the Nueber's rule was used here to determine the stress concentrations produced by microscopic discontinuities, that are a part of the materials microstructure, from directly measured remote and local strains.

Remote stresses and strains were determined. Local strains were directly measured. Local stresses were calculated by putting the local strain values into Equation 9, along with the appropriate constants from Table 5. The measured strains and calculated stresses for the discontinuities are listed in Table 6. All of the parameters, necessary to determine the stress concentrations around the discontinuities using the Nueber relationship, (Equation 10) have been directly measured or calculated. The stress concentrations for the corresponding discontinuity are also listed in Table 6.





Table 6. Local strains, local stresses and stress concentrations around discontinuities

Discontinuity	$\Delta\epsilon/2$	$\Delta\sigma/2$	$K_t$
170 BHN specimen			
shrinkage	.00272	54	1.75
nodule	.00210	49	1.47
nodule	.00175	44	1.27
nodule	.00175	44	1.27
nodule	.00230	50	1.55
nodule	.00170	44	1.25
nodule	.00202	48	1.42
nodule	.00200	47	1.40
nodule	.00190	46	1.35
250 BHN specimen			
nodule	.00155	47	1.26
nodule	.00150	46	1.23
nodule	.00155	47	1.26
nodule	.00170	50	1.36
nodule	.00155	47	1.26



Theoretical stress concentration factors ( $K_t$ ) for ellipsoidal cavities<sup>(17)</sup> are illustrated in Figure 28. These values are for a cavity in an infinite body in tension. The ellipsoid is defined by two radii,  $r$  and  $t$ . The stress concentration is plotted against the ratio of the two radii  $t/r$ .

If the shape of the nodules or shrinkages is approximated by an ellipsoid, the ratio of  $t/r$  would vary from 1 to 3, as determined from microscopy. The corresponding theoretical stress concentrations would be between 2 and 3. These values are nearly twice the values experimentally determined in this study.

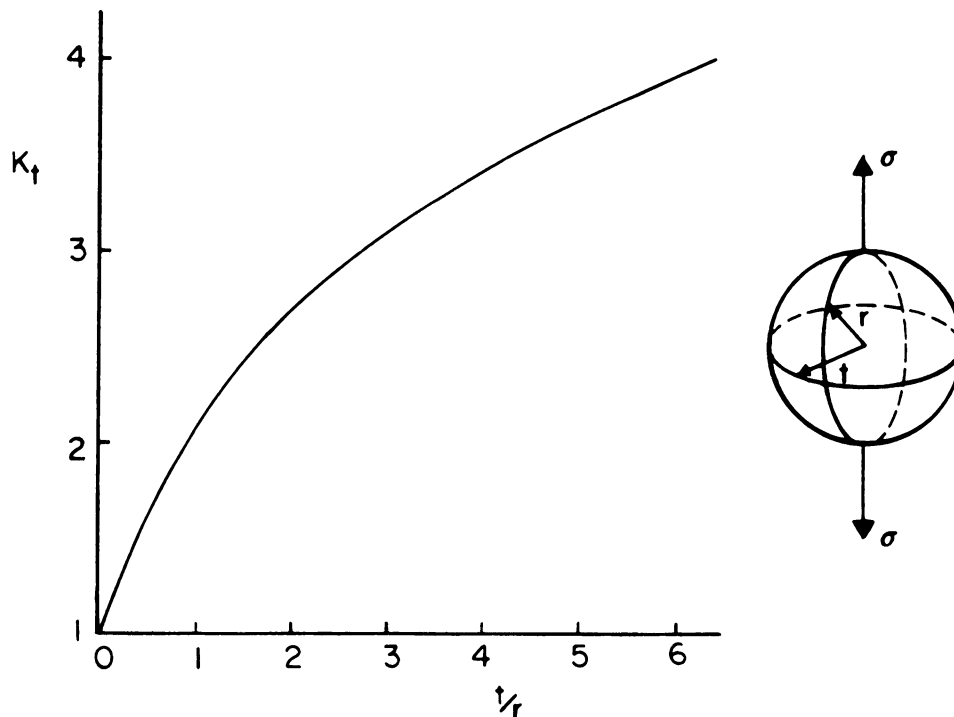
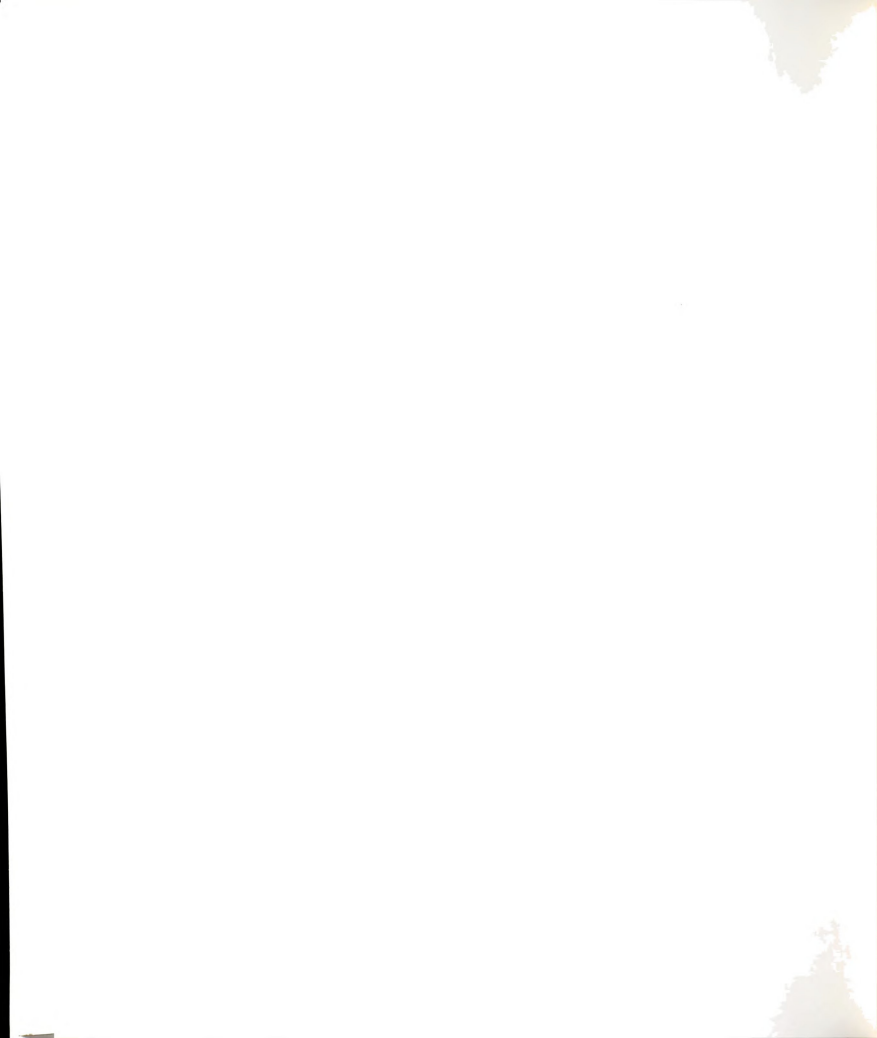


Figure 28. Theoretical stress concentrations from an ellipsoidal cavity



The difference between the theoretical and experimental values may be partially attributed to the location of the indentations. The minimum gage length used (75  $\mu\text{m}$ ) was not small enough to place the indentations at the notch root of the graphite nodules. This can be seen in Figure 23. The shrinkages were larger so the indentations were closer to the notch root. Stress concentrations measured near the shrinkages were closer to the theoretical values than those measured around the nodule.



## CHAPTER 5

### CONCLUSIONS

Strain-life behavior of four hardness ranges of pearlitic malleable iron have been determined. Pearlitic malleable iron is generally a cyclic softening material between the hardness ranges of 170 and 250 BHN. All hardness ranges soften except the lowest hardness range which slightly hardens. Because of this, the difference in stress-strain response between hardness ranges, decreases as this material is cycled. This causes the strain life properties to be less sensitive to hardness than the monotonic properties. However, this material does exhibit a trend in which the strain-life becomes shorter with decreasing hardness. This trend is observed at all strain amplitudes unlike common steels which have strain-life curves, for different hardness ranges, that cross at the transition fatigue life.

The strain-life behavior of pearlitic malleable iron is more reliable than many cast irons. The scatter in these data was small for a cast iron. Much of the scatter, that was observed, was produced by inaccurate nondestructive methods of categorizing this material. Microshrinkages often initiate failures but they do not appear to substantially shorten the fatigue lives.

The variation in strains between microstructural discontinuities and the matrix have been measured. The macroscopic cyclic behavior of pearlitic malleable iron is produced by the strength of the matrix, combined with the stress concentrations caused by the discontinuities. This is verified by the strain measurements which show the macroscopic





strains to be greater than the strains measured in the matrix but less than the strains measured around discontinuities.

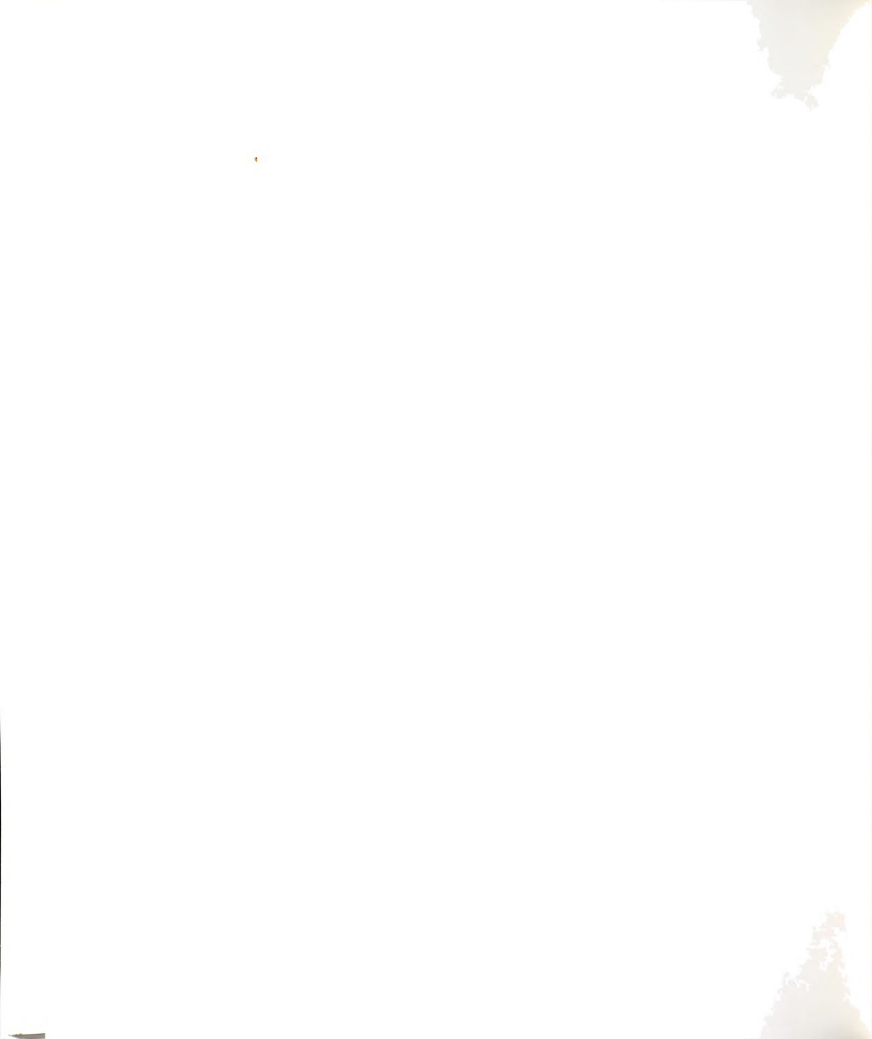
Stress concentrations have been calculated for microscopic discontinuities in this material, using direct strain measurements. Table 6 shows these stress concentrations to be small and consistently small for all regions tested and for both hardnesses extremes tested.

The strain-life behavior of pearlitic malleable iron is a product of the composite response of the matrix and the graphite nodules. This material has a more stable cyclic stress-strain response, with respect to changes in hardness, than a monotonic response. Graphite nodules produce relatively low stress concentrations. The high quality of the castings combined with these properties produce a strain-life response which has low scatter and is relatively insensitive to hardness. In conclusion, pearlitic malleable iron has excellent strain-life behavior for a cast iron.



## LIST OF REFERENCES

1. Gilber, G. N. J., "Review of Recent Properties of Nodular Cast Iron," Foundary Trade Journal, May 19, 1966, pp. 667-672, May 26, 1966, pp. 713-723.
2. Testin, R. A., "A Review of the Mechanical Properties of Nodular Cast Iron with Special Reference to Fatigue," T. A. M. Report No. 2, Department of Theoretical and Applied Mechanics, University of Illinois, Urbana, Illinois, 1972.
3. Socie, D. F., Fash, J. W., and Downing, S. D., "Fatigue of Gray Iron," T. A. M. Report No. 44. Department of Theoretical and Applied Mechanics, University of Illinois, Urbana, Illinois, 1982.
4. "Properties and Selection: Irons and Steels," Metals Handbook, American Society of Metals, 9th Ed., Vol. 1, Metals Park, Ohio, 1982, pp. 57-73.
5. Mitchell, M. R., "Effects of Graphite Morphology, Matrix Hardness and Structure on the Fatigue Resistance of Gray Iron," T. A. M. Report No. 14, Department of Theoretical and Applied Mechanics, University of Illinois. Urbana, Illinois, 1974.
6. Testin, R. A., "Characterization of the Cyclic Deformation and Fatigue Behavior of Nodular Cast Iron," Fracture Mechanics Report No. 371, Department of Theoretical and Applied Mechanics, University of Illinois, Urbana, Illinois, 1973.
7. Ikawa, K., Ohira, G., "Fatigue Properties of Cast Iron in Relation to Graphite Structure," American Foundary Society, Cast Metals Res. J., Vol 3, 1976, pp. 11-21.
8. "Malleable Iron Castings," Malleable Founders Society, Cleveland, Ohio, 1960, 57-75.
9. Angus, H. T., "Cast Iron: Physical and Engineering Properties," Butterworths Inc., Boston, Massachusetts, 1976, pp. 187-199.
10. "Nondestructive Inspection and Quality Control," Metals Handbook, American Society of Metals, 8th Ed., Vol. 11, Metals Park, Ohio, 1976, p. 426.
11. Feltner, C. E., Mitchell, M. R., "Basic Research on the Cyclic Deformation and Fracture Behavior of Materials," ASTM STP 465, American Society of Testing Materials, 1969, pp. 27-66.
12. Hirschberg, M. H., "A Low Cycle Fatigue Testing Facility," Manual on Low Cycle Fatigue, ASTM STP 465, American Society of Testing Materials, 1969, pp. 67-86.



13. Webster, J. T., "An Investigation to Determine the Reliability of the Brinell Test and Some Nondestructive Tests in Quality Testing Gray Iron-Castings," M. S. Thesis, Department of Mechanical Engineering, Michigan State University, 1964.
14. Topper, T. H., Wetzel, R.M., and Morrow, J. "Neuber's Rule Applied to Fatigue of Notched Specimens," Journal of Materials, Vol. 4, No. 1, March 1969, pp. 200-209.
15. Bofferding, C. H. III, "A Study of Cyclic Stress and Strain Concentration Factors at Notch Roots Fatigue Life," M. S. Thesis, Department of Metallurgy, Mechanics and Materials Science, Michigan State University, 1980, pp.4-18.
16. Sharpe, W. N. Jr., "A Short Gage Length Optical Gage for Small Strain," Experimental Mechanics, Vol. 14, No. 9, 1971, pp. 373-377.
17. Peterson, R. E., Stress Concentration Factors, Wily, New York, 1974, pp.139-141, 219.



MICHIGAN STATE UNIVERSITY LIBRARIES



3 1293 03047 1381